Programmable super-resolution pupil phase filter with a deformable mirror

Lina Zhao (赵丽娜)[1,2,3,4,5], Yun Dai (戴 云)[1,4,*], Junlei Zhao (赵军磊)[1,4,5], Fei Xiao (肖 飞)[1,4], Xiaojun Zhang (张小军)[1,4], Xiaojun Zhou (周晓军)[2], and Yudong Zhang (张雨东)[1,4]

[1]*The key laboratory on Adaptive Optics, Chinese Academy of Science, Chengdu 610209, China*
[2]*University of Electronic Science and Technology of China, Chengdu 610054, China*
[3]*Chengdu University of Information Technology, Chengdu 610225, China*
[4]*Institute of Optics and Electronics, Chinese Academy of Sciences, Chengdu 610209, China*
[5]*University of Chinese Academy of Sciences, Beijing 100049, China*
**Corresponding author: daiyunqq@163.com*

Received April 14, 2016; accepted July 22, 2016; posted online August 31, 2016

Compared with binary diffractive super-resolving elements, programmable super-resolution pupil filters permit the analysis of various filter designs and allow the filters to be changed rapidly to modify the response of an optical system. In this Letter, a deformable mirror is employed as a programmable super-resolution pupil phase filter. Continuous phase-only filters based on the Zernike polynomial series are designed by the genetic algorithm and fitted through closed-loop adaptive optics with a piezoelectric deformable mirror. Experimental super-resolution results are in agreement with the theoretical predictions. This method has no polarization light requirement and is convenient for application.

OCIS codes: 120.5060, 350.4600, 350.5730.
doi: 10.3788/COL201614.091201.

Optical super-resolution research based on pupil filter has been stimulated by the work of Toraldo di Francia[1] that makes the connection between super-directive antennas and super-resolving pupil filters. The main strategy is placing a filter at the exit pupil of an optical system to properly modify the diffracted pattern. The existing investigation can be roughly divided into three categories: the research on the types of super-resolving pupil filters, namely, amplitude-only type[2–4], phase-only type[5], or amplitude-phase type[6]; the profile functions of super-resolution pupil filters, continuous function filters[6], or discrete ones[7]; the applications of super-resolution techniques, such as optical data storage[8], astronomy[9], confocal microscopy[10], and nanolithography[11]. An alternative approach for optical super-resolution is to utilize the vector feature of the light beam[12–15]. The central lobe is always accompanied with the side lobe effect for filter-based super-resolution[16]; some valuable methods based on the nonlinear effects[11,17] have been proposed to remove or decrease the side lobe effect.

Most super-resolution pupil filters are made of binary elements, mainly because of their simple structure. By changing the values of zone boundaries or/and phase or amplitude transmittance of the binary element, a desired diffraction pattern can be directly characterized. However, the practical implementation of conventional binary elements has been hampered by structural complexity, invariability, and extremely tight tolerances.

In subsequent years, some studies demonstrated that a liquid-crystal spatial light modulator (LCSLM) can also serve as a super-resolution pupil filter to overcome the limits of the binary elements. When addressed by a programmed light intensity distribution, LCSLM allows high frequency light modification in various phase or amplitude modes. In 1992, Freeman *et al.*[18] performed phase-only modulation by employing a ferroelectric LCSLM. However, this LCSLM suffered from low efficiency. In 1999, Davis *et al.*[2] showed how to program various transmission filters by using a programmable LCSLM that operated in an amplitude-only mode. In 2003, McOrist *et al.*[5] used an optically addressable parallel-aligned pneumatic LCD to generate a phase-only filter. Both of the above experiments resulted in success.

However, a polarization light is needed for the LCSLM to be used as a super-resolution filter, which is a severe restriction for the application. Here we employ a deformable mirror (DM) as a phase-only filter to improve resolution. To the best of our knowledge, this is rarely covered in the existing literature in terms of both theoretical analysis and experimental demonstration.

A DM is commonly used as the correcting mirror in an ocular adaptive optics (AO) system[19]. In this study, the potential of a DM as the diffractive optical element (DOE) for programmable phase-only correlation filters bears several advantages. The first is fabrication. Prior knowledge suggests that continuous phase-only filters can produce better super-resolution results; however, continuous patterns are more difficult to fabricate, especially for binary elements. The DM offers a means to accomplish a complex continuous structure without tight tolerance. The second motivation is fewer limits. From a practical point of view, there are no special treatments on beacon light source for DM super-resolution optical systems, a feature not available for LCSLM filters. The third relevant motivation is

programmability. If super-resolution elements are to find widespread applicability, it is necessary to possess not only satisfactory performance, but also a significant flexible structure. Using the DM as a super-resolution filter permits the analysis of various filter designs, and allows the filters to be changed rapidly to modify the response of an optical system at high efficiency. Although the design process becomes more mathematically involved, it is not difficult to reach an excellent solution.

In order to fit the pupil phase with high accuracy, a 145-element PZT DM based on 3 mm spacing piezoelectric actuators recently made by our labs is employed here. The 3 mm spacing piezoelectric actuators were based on the characteristic of d31 in PZT and made it possible to develop a multiple element DM with a small aperture. The clear aperture size of the 145-element DM was optimized to 35 mm in diameter, and its electrode distribution is shown in Fig. 1(a). The influence function of a central actuator measured by a Veeco interferometer is shown in Fig. 1(b). From the measured influence function, the coupling of the central actuator, which is the ratio of the deformation of the neighboring actuator to that of the central actuator, was 14%. The range of the driving voltage of the DM was ±500 V and the stroke was ±2 μm.

Based on the layout of actuators and the measured influence function, a simulation analysis of the correction capability of wave-front error was first conducted. As shown in Fig. 1(c), the first 45 Zernike modes could be corrected effectively by the DM, which was successfully used to correct ocular aberrations for high resolution retinal imaging[20].

A particular issue that must be addressed is how to make the DM fit the designed pupil filter profile. Let us first briefly describe the method to find the actuating voltage of the DM in an AO system. As is well known, the Shack-Hartmann wave-front sensor (SHWS) divides the incident wave-front into a number of sub-apertures. The light through each sub-aperture is brought into focus in the focal plane of the lenslet array. The ideal plane wave results in a regular array of focus spots. Each spot is located on the optical axis of the corresponding lenslet. This plane wave pattern will be used as a reference pattern. If a deformed wave-front is measured, the image spot at each sub-aperture shifts with respect to the corresponding point in the reference pattern by a factor proportional

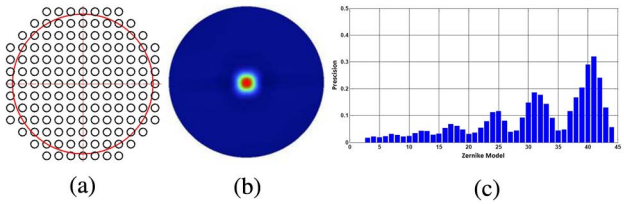

Fig. 1. (a) Actuators arrangement, (b) the experimental measured influence function, and (c) the correction capability of wave-front errors of the 145-element PZT DM.

to the local tilt. The local slopes of the wave-front can therefore be detected by the measurement of the shift of the focus spots. Using the direct slope control algorithm[21], the correction voltage of the DM is computed by

$$V = C \cdot S, \tag{1}$$

where V is the actuating voltage vector of the DM, C is the control matrix of the AO system, and S is the wave-front slope vector of SHWS, which is described by

$$S = \frac{C_i - C_{\text{ref}}}{\lambda f} = S_i - S_{\text{ref}}, \tag{2}$$

where C_i is the centroid position of incident wave-front, C_{ref} is the reference centroid position, λ is the wavelength of incident light beam, and f is the focal length of the lenslet. Simply, S can be calculated by the difference in values between the incident wave-front slope vector S_i and the reference slope vector S_{ref}.

The pupil filter phase based on Zernike polynomials is described by a group of Zernike coefficients A_f. Based on the SHWS wave-front reconstruction theory, the corresponding slope vector can be expressed as

$$S_f = R^{-1} \cdot A_f, \tag{3}$$

where S_f is the slope vector of pupil filter phase, and R^{-1} is the generalized inverse of the SHWS reconstruction matrix. To make the DM fit the required pupil filter phase, it only needs to modify the reference slope vector of SHWS by

$$S'_{\text{ref}} = S_{\text{ref}} - S_f. \tag{4}$$

By replacing the original reference slope vector with modified ones, the closed-loop fitting of the pupil filter phase can easily be achieved as a conventional AO system. Moreover, there is no excess computational burden for a closed-loop AO system because the modification process of the reference slope vector can be calculated in an offline mode.

A pupil function $P(\rho)$ is usually considered as a combination of phase and amplitude which can be written as

$$P(\rho) = A(\rho) \cdot \exp[i \cdot \varphi(\rho)], \tag{5}$$

where ρ is the normalized radius over the circular pupil. The filter is characterized by the amplitude transmittance $A(\rho)$ and the phase function $\varphi(\rho)$. Super-resolution techniques differ in the way the functions $A(\rho)$ and $\varphi(\rho)$ are defined and optimized. Our strategy is based on the control of the continuous phase function $\varphi(\rho)$ so that they can be reproduced by a DM.

The general modification procedure is used to expand the pupil function in some complete set of functions and adjust the coefficients to approximate the prespecified point spread functions (PSFs). Because Zernike polynomials are orthogonal over a unit circle, they are usually

used as a representation of the wave-front phase. Meanwhile, PZT DM is characterized by non-locality. This means that the voltage applied to an electrode at one point can affect the surface deformation at all points. For these two main reasons, the phase function $\varphi(\rho)$ can then be mathematically described as the weighted sum of Zernike basis functions

$$\varphi(\rho) = \sum_m c_m z_m(\rho, \theta), \tag{6}$$

where z_m is the mth term of the Zernike polynomial series, and c_m is their respective coefficients that are to be determined. By changing the values of the coefficients, different phase pupil filters can be generated.

Considering that our 145-element DM could correct the first 45 Zernike modes effectively and the rotationally symmetric characteristic of super-resolution filter, the phase pupil filter function is expressed as

$$\varphi(\rho) = c_4 z_4 + c_{12} z_{12} + c_{24} z_{24} + c_{40} z_{40}, \tag{7}$$

where

$$\begin{cases} z_4 = \sqrt{3}(2\rho^2 - 1) \\ z_{12} = \sqrt{5}(6\rho^4 - 6\rho^2 + 1) \\ z_{24} = \sqrt{7}(20\rho^6 - 30\rho^4 + 12\rho^2 - 1) \\ z_{40} = \sqrt{9}(70\rho^8 - 140\rho^6 + 90\rho^4 - 20\rho^2 + 1) \end{cases}. \tag{8}$$

The next step is to seek coefficients c_m that lead to a super-resolution phase function $\varphi(\rho)$. Our design method consists of defining a series of figures of merit that when properly used will provide the coefficients c_m that describe the phase-mask shape. The critical figures of merit that we have taken into account are the Strehl ratio (S) and the transverse super-resolution gain factor (G_T). S is a relevant parameter for analyzing image quality and is defined as the ratio between the intensity of the super-resolved pattern and that of the Airy pattern at the focal point. G_T gives a measure of the super-resolution performance and is defined as the ratio of the position of the first zero of intensity for the Airy pattern to that for the super-resolution pattern. From literature[22], the analytical expressions of these two figures of merit can be written as

$$S = |I_0|^2 + \frac{1}{2}\,\mathrm{Im}(I_0^* I_1) u_F, \tag{9}$$

$$G_T = 2\frac{\mathrm{Re}(I_0 I_1^*) + \frac{1}{2} u_F\,\mathrm{Im}(I_0^* I_2)}{S}, \tag{10}$$

where I_n is the nth moment of the pupil function, and defined as

$$I_n = 2\int_0^1 P(\rho)\rho^{2n+1}\mathrm{d}\rho, \tag{11}$$

and u_F is small displacements of the focus position from the geometrical focus

$$u_F = 2\frac{\mathrm{Im}(I_0 I_1^*)}{\mathrm{Re}(I_2^* I_0) - |I_1|^2}. \tag{12}$$

In our analysis, the structure coefficients c_m of the optimal filter will be fitted to fulfill restrictive conditions such as a limited displacement of the focus position, a high Strehl ratio, and a transverse super-resolution gain factor at least larger than a unit. As a consequence, the four coefficients in Eq. (7) are obtained from the following system of equations:

$$\text{Maximize } G_T(c_4, c_{12}, c_{24}, c_{40}) \quad \text{subject to } \begin{cases} |u_F(c_4, c_{12}, c_{24}, c_{40})| \le u_F^0 \\ S(c_4, c_{12}, c_{24}, c_{40}) \ge S^0 \end{cases}, \tag{13}$$

where u_F^0 is the constrained displacement of the focus, and S^0 is the constrained spot intensity. The genetic algorithm (GA) is one of the ideal methods for solving this system of equations. As the name suggests, a GA operates on the principle of natural selection. To find the best filter shape, a typical GA begins with an initial population. For each member of the population, the algorithm evaluates the ability to meet the design goals or fitness. Based on fitness, the algorithm chooses members to become parents to be the elite for a new generation. The algorithm applies operators to the parents to mix their chromosomes into children and simply retains the elite. Finally, the algorithm combines children and elite into a new population, and subjects them to the same process as their predecessors. The algorithm continues this natural selection until it times out or the population meets a fitness goal.

Under the constrained condition of u_F^0 as 10 and S^0 as 0.25, a few minutes or even ten minutes were needed to obtain a family of optimum coefficients using a computer with an Intel Core i5-5200U CPU at 2.20 GHz. Table 1 presents two examples from the family corresponding to two particular filters. For each group of solutions, the values of u_F, G_T, and S are given. Furthermore, the axial super-resolving gain G_A is presented, which indicates a

Table 1. Performance of Phase Filters with the Form $\varphi(\rho) = c_4 z_4 + c_{12} z_{12} + c_{24} z_{24} + c_{40} z_{40}$

	Coefficients				Figures of Merit			
Filter	C_4	C_{12}	C_{24}	C_{40}	u_F	S	G_T	G_A
1	1.0496	−0.7565	0.2935	−0.0007	5.9000	0.3880	1.3333	1.1106
2	−0.1365	0.8358	−0.2225	−0.1992	1.2500	0.4780	1.0909	0.6228

measure of the super-resolution performance in the axial direction and is defined as the ratio of the position of the first minimum of intensity for the Airy pattern to that for the super-resolution pattern along the optical axis. This figure of merit is used here to check the three dimensional super-resolution performances of our different phase filters.

With the figure of merits varying with coefficients as shown in Table 1, it is clear that each G_T is larger than a unit. This means that both filters have a transverse super-resolution performance. Moreover, Table 1 shows that filter1 has a higher G_T, while filter2 has a higher S. For filter1, both G_T and G_A are larger than 1, which demonstrates that filter1 has a three-dimensional super-resolution performance, a feature not available for filter2.

Using the coefficients c_m in Table 1, we reconstruct the pupil profiles of filter1 and filter2, and their transverse curves are shown in Figs. 2(a) and 2(b). Furthermore, the latter four sub-figures of Fig. 2 illustrate a normalized intensity distribution of the two filters. The dashed lines correspond to uniform transmission. The solid lines in Figs. 2(c) and 2(d) are the transverse intensity distributions of filter1 and filter2, respectively. While the solid and marked lines in Figs. 2(e) and 2(f) depict the axial intensity distribution of filter1 and filter2, respectively.

Table 1 and Fig. 2 illustrate that with different coefficient groups of c_m, the pupil filter will present various super-resolving performances. The Strehl ratio of filter1 is smaller than that of filter2, while both the transverse super-resolving gain G_T and axial super-resolving gain G_A of filter1 are larger than those of filter2. This means that, as a rule, the improvement of the resolution is accompanied by the loss of the central lobe intensity. High gain values are obtained at the cost of a low Strehl ratio, which is in accordance with the super-resolution theory. The super-resolution performance can be revised by properly choosing the designing parameters of c_m.

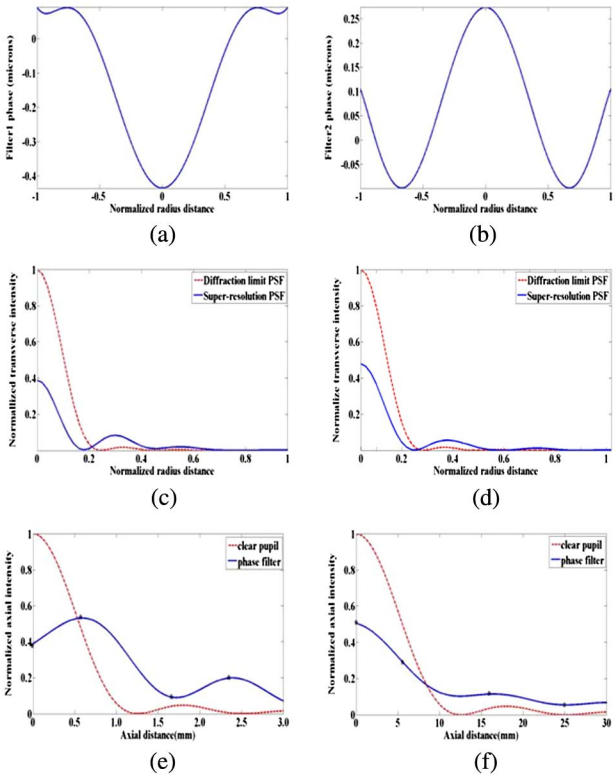

Fig. 2. Transverse curve of the pupil profiles of (a) filter1 and (b) filter2, the normalized transverse intensity distribution of (c) filter1, and (d) filter2, and the axial intensity distribution of (e) filter1 and (f) filter2 compared with that of Airy spot.

The schematic of experimental setup is shown in Fig. 3. A collimated visible beam with a wavelength of 638 nm, as beacon light source, illuminates the 145-element PZT DM. The beam is modulated in phase by that DM. The modulated beam is relayed and condensed from 35 to 6.5 mm by a set of spherical mirrors, passed through a beam splitter, and divided into two branches. One branch is measured with an SHWS consisting of a 16×16 lenslet array (f is 15 mm; lenslet diameter is 0.4 mm), which samples the exiting wave-front across a 6.5 mm pupil. The other one is focused by a lens with a focal length of 200 mm and a diameter of 26 mm. The diameter of light for focus is 6.5 mm, and the corresponding NA for focus is 0.016. The focused spot is magnified with a 40× microscope objective and imaged onto a detector. A CCD camera (View Works Inc., Korea) with 795×596 pixels is used as the detector. The point spread intensity is obtained at the CCD location which is the focal plane of the optical system. To examine various defocusing planes, we fix the distance between the microscope objective and detector and translate the entire objective-detector system.

A closed-loop AO system is used to generate an arbitrary phase pattern by entering the modified SHWS centroid locations as input to the AO controller. The centriod locations are computed in Matlab for our above defined phase pattern, allowing us to test the ability of the DM to generate various pupil filter phases.

Before conducting the experiment, the filter profiles are numerically fitted based on the measured influence function to evaluate the feasibility of the 145-element PZT DM for pupil phase filters. Figures 4(a) and 4(b)

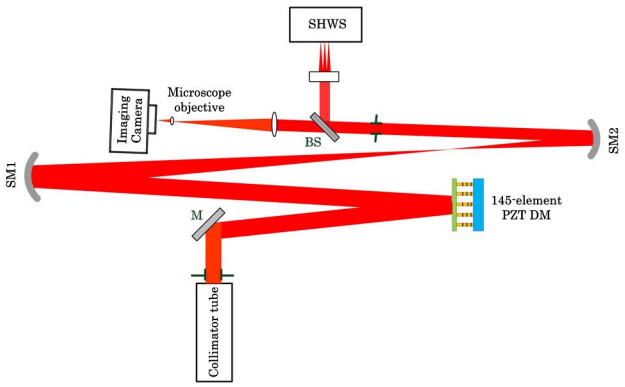

Fig. 3. Experimental setup for attaining phase modulation using a 145-element PZT DM.

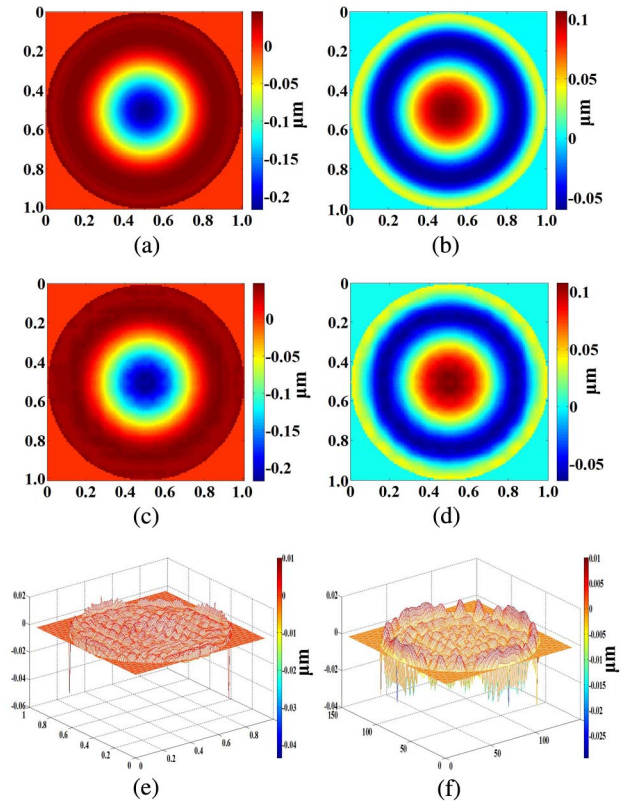

Fig. 4. Expected filter profiles of (a) filter1 and (b) filter2, the fitted profiles of (c) filter1 and (d) filter2, and the fitting residual errors of (e) filter1 and (f) filter2.

are the expected profiles of filter1 and filter2, respectively. Considering the reflective use of the DM, only half of the designed phase values of filters need to be fitted by the DM. Figures 4(c) and 4(d) are the fitted profiles by the DM, and Figs. 4(e) and 4(f) are the fitted residual errors of filter1 and filter2, respectively. The residual root mean square (RMS) error of filter1 and filter2 are 0.0016 and 0.0031 μm, respectively.

The experimental results of transverse intensity distribution at the geometrical focal plane are depicted in Fig. 5. Figure 5(a) is the experimental results of the Airy pattern, Fig. 5(b) and 5(c) are those of filter1 and the filter2, respectively.

It is clear that each intensity distribution has a relative high intensity central spot surrounded by a lower intensity ring, as shown in Fig. 5. With the super-resolution filter1 or filter2, the center lobe of the transverse intensity becomes smaller and more ambiguous than that of the original optical system. It means that the high transverse resolution is obtained at the cost of the central intensity loss. It also shows that filter1 [Fig. 5(b)] results in lower intensity side-lobes than that of filter2 [Fig. 5(c)], this effect is only a consequence of the smaller PSF reduction obtained.

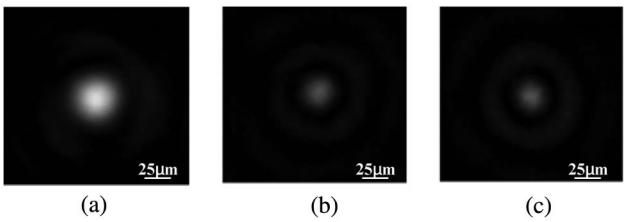

Fig. 5. Experimental measurements of the intensity distribution at the geometrical focal plane obtained from (a) free pupil, (b) super-resolution filter1, and (c) super-resolution filter2.

Furthermore, in Fig. 6, the horizontal cross curves of the three focused spots in Fig. 5 are presented for comparing the experimental values with the theoretical computations. The small block diagram is the magnified curve located in the position of the first zero of intensity of the filters. The dotted line, the solid line, and the dashed line correspond to Figs. 5(a), 5(b), and 5(c), respectively. Each S and G_T of the filters is recalculated according to their physical definition. In Fig. 6, the S is 0.3776 and 0.4764, and the G_T is 1.322 and 1.105, corresponding to filter1 and filter2, respectively. The experimental results agree with the theoretical predictions that are shown in Table 1 with an absolute error of less than 0.01.

Moreover, Fig. 7 shows two-dimensional intensity distributions in different axial planes. Fig. 7(a) is the axial super-resolution behavior of filter1. The positions of these

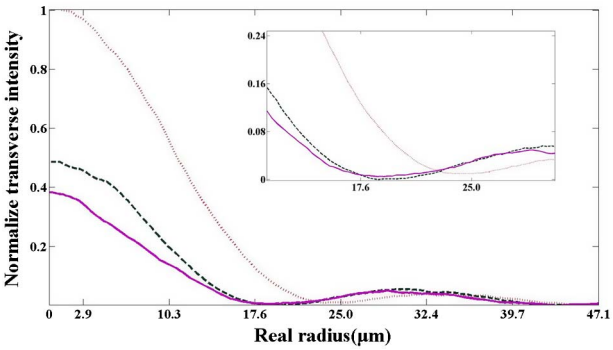

Fig. 6. Horizontal cross curves of Fig. 5.

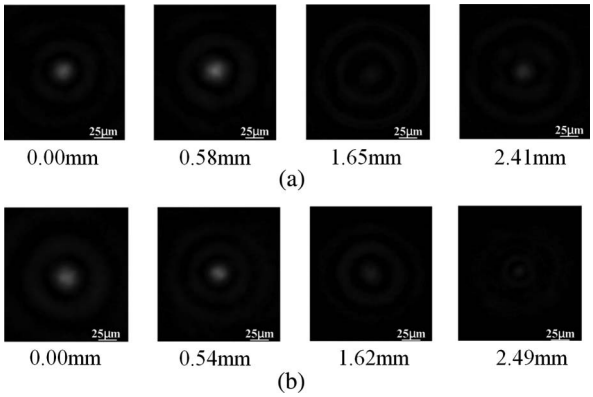

Fig. 7. Experimental measurements of two-dimensional intensity plots at different axial positions marked in Figs. 2(e) and 2(f): (a) filter1, (b) filter2.

planes coincide with those that are marked with an asterisk in Fig. 2(e). The axial intensity increases and then diminishes to form sequential focuses at different axial distances. The intensity oscillation behavior of this filter is clearly shown.

Again, Fig. 7(b) is the two-dimensional intensity distributions at four axial positions of filter2. The positions of these planes correspond to those that are marked with an asterisk in Fig. 2(f). In this case, the axial intensity continuous to decrease slowly, which is different than those of the axial performance of filter1. The experimental results are in agreement with the theoretical predictions of Fig. 2(f). It is possible for super-resolution filters to achieve both transverse super-resolution and extension of depth of focus (DOF).

The above intensity variety in the focal plane and along the optic axis of filter1 and filter2 are totally different principally due to the distinct filter coefficients of Eq. (7). Consequently, by changing the values of the coefficients, a DM can generate different super-resolution effects to meet various applications.

In conclusion, we introduce the DM as a programmable filter to achieve super-resolution performance. Respecting various special demanding merits of filters, suitable phase-only masks are obtained by using the GA optimization procedure. As an example, a 145-element DM is used successfully to generate two special phase-only masks. The PSFs of two filters in the focal plane with different continuous phase-only masks clearly demonstrate a reduction in the width of the central lobe. In addition, the axial super-resolution behaviors of two filters are analyzed too. They demonstrate that filter1 has a three-dimensional super-resolution performance, and filter2 has a higher Strehl ratio. The experimental results are consistent with previous theoretical predictions.

The DM, acting as a potent super-resolution pupil filter, can be operated in a continuously variable phase-only mode at high efficiency, and can be controlled dynamically. This method is straightforward, analytical, and simple. The technique is easy to implement and allows us to flexibly control the desired PSF characteristics.

This work was supported by the National Natural Science Foundation of China (No. 61378064) and the National High Technology Research and Development Program of China (No. 2015AA020510). The authors thank Professor Wenhan Jiang for his critical comments. Useful discussions from our group are acknowledged.

Reference

1. G. T. D. Francia, IL Nuovo Cimento **9**, 426 (1952).
2. J. A. Davis, J. C. Escalera, J. Campos, A. Marquez, M. J. Yzuel, and C. Lemmi, Opt. Lett. **24**, 628 (1999).
3. Y. Zha, J. Wei, H. Wang, and F. Gan, J. Opt. **15**, 075703 (2013).
4. J. Wei, Y. Zha, and F. Gan, Prog. Electromagn. Res. **140**, 589 (2013).
5. M. D. Sharma, J. McOrist, C. J. R. Sheppard, and K. Matsuda, Proc. SPIE **4829**, 292 (2003).
6. V. F. Canales, P. J. Valle, J. E. Oti, and M. P. Cagigal, Chin. Opt. Lett. **7**, 720 (2009).
7. G. Xiumin, F. Gan, and W. Xu, Opt. Laser Technol. **39**, 5 (2007).
8. Y. Junjie, C. Zhou, and W. Jia, Opt. Commun. **283**, 21 (2010).
9. V. F. Canales, D. M. D. Juana, and M. P. Cagigal, Opt. Lett. **29**, 935 (2004).
10. Y. Ding, H. Xie, T. Peng, Y. Lu, D. Jin, J. Teng, Q. Ren, and P. Xi, Opt. Express **20**, A13 (2012).
11. Y. Zha, J. Wei, and F. Gan, Opt. Commun. **304**, 49 (2013).
12. Z. Nie, G. Shi, X. Zhang, Y. Wang, and Y. Song, Opt. Commun. **331**, 87 (2014).
13. Z. Nie, G. Shi, D. Li, X. Zhang, Y. Wang, and Y. Song, J. Modern Opt. **62**, 67 (2015).
14. Z. Nie, G. Shi, D. Li, X. Zhang, Y. Wang, and Y. Song, J. Opt. **17**, 055605 (2015).
15. Z. Nie, W. Ding, G. Shi, D. Li, X. Zhang, Y. Wang, and Y. Song, Opt. Express **23**, 21296 (2015).
16. V. F. Canales, P. J. Valle, and M. P. Cagigal, Chin. Opt. Lett. **14**, 071101 (2016).
17. Y. Zha, J. Wei, and F. Gan, Opt. Commun. **293**, 139 (2013).
18. M. O. Freeman, T. A. Brown, and D. M. Walba, Appl. Opt. **31**, 3917 (1992).
19. Y. Yu and Y. Zhang, Chin. Opt. Lett. **12**, 121202 (2014).
20. J. Zhao, F. Xiao, J. Kang, H. Zhao, Y. Dai, and Y. Zhang, J. Innovative Opt. Health Sci. **10**, 1650038 (2016).
21. J. Wenhan and L. Huagui, Proc. SPIE **1271**, 82 (1990).
22. D. M. de Juana, J. E. Oti, V. F. Canales, and M. P. Cagigal, Opt. Lett. **28**, 607 (2003).